

Article

# Preliminary Characterization of Glass/Alumina Composite Using Laser Powder Bed Fusion (L-PBF) Additive Manufacturing

Byeong Hoon Bae <sup>1</sup>, Jeong Woo Lee <sup>1</sup>, Jae Min Cha <sup>1</sup>, Il-Won Kim <sup>1</sup>, Hyun-Do Jung <sup>2,\*</sup>  and Chang-Bun Yoon <sup>1,\*</sup>

<sup>1</sup> Department of Advanced Materials Engineering, Korea Polytechnic University, Siheung-si 15073, Korea; bbhqoqod@naver.com (B.H.B.); jungwoo.618@daum.net (J.W.L.); woals4102@naver.com (J.M.C.); ilwon5709@naver.com (I.-W.K.)

<sup>2</sup> Department of BioMedical-Chemical Engineering (BMCE), The Catholic University of Korea, Bucheon 14662, Korea

\* Correspondence: hdjung@catholic.ac.kr (H.-D.J.); cbyoon@kpu.ac.kr (C.-B.Y.); Tel.: +82-2-2164-4357 (H.-D.J.); +82-31-8041-0589 (C.-B.Y.)

Received: 22 March 2020; Accepted: 1 May 2020; Published: 7 May 2020



**Abstract:** Powder bed fusion (PBF) additive manufacturing (AM) is currently used to produce high-efficiency, high-density, and high-performance products for a variety of applications. However, existing AM methods are applicable only to metal materials and not to high-melting-point ceramics. Here, we develop a composite material for PBF AM by adding Al<sub>2</sub>O<sub>3</sub> to a glass material using laser melting. Al<sub>2</sub>O<sub>3</sub> and a black pigment are added to a synthesized glass frit for improving the composite strength and increased laser-light absorption, respectively. Our sample analysis shows that the glass melts to form a composite when the mixture is laser-irradiated. To improve the sintering density, we heat-treat the sample at 750 °C to synthesize a high-density glass frit composite. As per our X-ray diffraction (XRD) analysis to confirm the reactivity of the glass frit and Al<sub>2</sub>O<sub>3</sub>, we find that no reactions occur between glass and crystalline Al<sub>2</sub>O<sub>3</sub>. Moreover, we obtain a high sample density of ≥95% of the theoretical density. We also evaluate the composite's mechanical properties as a function of the Al<sub>2</sub>O<sub>3</sub> content. Our approach facilitates the manufacturing of ceramic 3D structures using glass materials through PBF AM and affords the benefits of reduced process cost, improved performance, newer functionalities, and increased value addition.

**Keywords:** powder bed fusion; additive manufacturing; 3D printing; glass/alumina composite; density; mechanical property

## 1. Introduction

The widely popular additive manufacturing (AM) approach based on 3D printing can be used to fabricate products with complex shapes and structures without needing a mold; in fact, some of these products cannot be fabricated with conventional molds [1–3]. However, 3D printing is mainly used for fabricating polymer and metal products rather than ceramics; the direct AM process cannot be applied to ceramics because they require high heat-treatment temperatures [4–7].

Meanwhile, ceramic materials are widely used in the construction, automotive, aerospace, electronics, biomedical, and chemical industries because of their excellent chemical resistance and hardness [8–10]. However, as ceramics have high melting points, it is difficult to manufacture complex structures using molds [11]. On the other hand, glass-ceramic materials exhibit high chemical stability, high transmittance, excellent hardness, and a relatively low melting temperature (<1400 °C); thus, they can be used to fabricate complex-shaped products by using molds and injecting glass. However,

the need for complex molds increases the manufacturing costs, thereby resulting in process limitations. Moreover, as glass ceramics are brittle and easily prone to breaking, their use is restricted to products requiring high toughness. Therefore, researchers are looking to harness 3D printing technologies to fabricate complex shapes [12–15].

The typical methods of fabricating AM-based 3D ceramic shapes include the stereolithography apparatus (SLA) method [16–18], in which a photocurable material is mixed in ceramics, and the binder-jetting method, which injects a binder on ceramic powder [7,19–24]. Both methods require polymers, and therefore, the standard approach involves the 3D-printing of a green body containing polymers and sintering by heat treatment after the burning out of the binder [25,26]. As the process of removing polymers is essential in conventional ceramic 3D printing, it is difficult to obtain a high-density, compact-structured sintered ceramic body; hence, there is an urgent need to develop a direct AM process for ceramics [27,28].

In this study, we fabricated a sintered ceramic-composite body through direct laser melting. We developed a powder bed fusion (PBF) 3D printing process in which a mixture of  $\text{Al}_2\text{O}_3$  and glass frit at a certain ratio is irradiated with a laser (L-PBF). Unlike a previous study by Datsiou et al. on L-PBF-based 3D printing using glass powder [29], here, we mixed low-melting-point glass frit and  $\text{Al}_2\text{O}_3$  to improve the mechanical properties by 3D-printing the composite using L-PBF. As  $\text{Al}_2\text{O}_3$  has a high melting point and does not melt with a laser, it was mixed with glass with a relatively low melting point, and 1 wt % to 3 wt % of black pigment was added to increase the absorption of laser light. Furthermore, to demonstrate the feasibility of our concept, we manufactured a scaffold by laser-irradiating the glass/ $\text{Al}_2\text{O}_3$  composite and sintering at 750 °C for 20 min to produce a high-density glass/ $\text{Al}_2\text{O}_3$  ceramic composite [30,31]. The resulting 70 wt % glass/30 wt %  $\text{Al}_2\text{O}_3$  composite exhibited a high hardness of 578 kg/mm<sup>2</sup> and density of 3.26 g/cm<sup>3</sup>.

## 2. Materials and Methods

Glasses based on a  $\text{SiO}_2$ – $\text{B}_2\text{O}_3$ –RO (R = Ba, Zn) ternary system were synthesized with a composite of  $\text{SiO}_2$  (25 mol%–40 mol%),  $\text{B}_2\text{O}_3$  (25 mol%–40 mol%), and RO (R = Ba, Zn) (20 mol%–35 mol%). The glasses were prepared via conventional melt quenching at 1400 °C for 1 h. After quenching, they were ground into powders and screened to under ~50 µm in size. The powders were packed into disks with diameters of ~15 mm and heat-treated at different temperatures. The amorphousness of the glasses was measured by means of X-ray diffraction (XRD) (D2 PHASER, Bruker Corporation, Billerica, MA, USA). To determine the optimum sintering temperature of the glasses, the transition and softening points were measured by means of differential thermal analysis (DTA) (DTA-50, Shimadzu, Kyoto, Japan). To select the appropriate heat treatment temperature for the specimens, after molding the glass powder, we observed the process of glass softening at 50 °C intervals using a high-temperature microscope (HTM, Pyrotech, Seoul, Korea) as the process temperature was raised from room temperature to 800 °C at 5 °C/min. The particle size distribution was measured by using a particle size analyzer (PSA) (Mastersizer 3000, Malvern, UK). As regards the raw material sourcing, we used a commercial high-purity  $\text{Al}_2\text{O}_3$  powder with  $D_{50}$  ~1 µm (>99.9%, High Purity Chemicals, Tokyo, Japan) to fabricate the glass composite, and black pigment (The Shepherd Color Company, Cincinnati, OH, USA) to increase the light absorption of the laser. To find the optimal mixing ratio, we mixed the glass and  $\text{Al}_2\text{O}_3$  powders at ratios of 90:10, 80:20, 70:30, 60:40, and 50:50 wt %. Subsequently, 1 wt % to 3 wt % of the black pigment was added to the samples. The mixture was thoroughly mixed by ball-milling with alumina balls at 110 rpm for 3 h.

We used a 1060 nm wavelength fiber laser (FLM-I/F, LPTech, Seongnam, Korea) to irradiate the glass- $\text{Al}_2\text{O}_3$  mixture samples with a 20 W laser to produce an 80 mm model, as shown in Figure 1a. The 3D-printed shape was heat-treated at 750 °C for 20 min to improve the density. Figure 1b shows the schematic of glass frit/ $\text{Al}_2\text{O}_3$  composite. To verify the surface properties, we observed the melting state of the surface using a scanning electron microscope (SEM) (Nova NanoSEM230, FEI, Hillsboro, OR, USA). In addition, the density of the sintered sample corresponding to each mixing ratio was

measured by means of the Archimedes method. The reactivity of glass and  $\text{Al}_2\text{O}_3$  was observed through X-ray diffraction (XRD). After sample polishing, hardness tests were conducted under a force of 2 kg for 5 s by using a Micro Vickers Hardness Tester (MVK-H200, Akashi, Tokyo, Japan). In the tests, 10 indentations were made per sample, and a total of 5 samples were used. The upper and lower bound of each hardness were calculated by the rule of mixtures combined Voigt and Reuss model, respectively [32]. According to Voigt model, the upper bound hardness,  $H_{\text{upper}}$  can be expressed as follow:

$$H_{\text{upper}} = f_{\text{glass}}H_{\text{glass}} + f_{\text{alumina}}H_{\text{alumina}},$$

where  $f_{\text{glass}}$  and  $f_{\text{alumina}}$  are the volume fractions of glass and  $\text{Al}_2\text{O}_3$ , respectively, and  $H_{\text{glass}}$  and  $H_{\text{alumina}}$  are the hardness of glass and  $\text{Al}_2\text{O}_3$ , respectively. According to Reuss model, the lower bound hardness,  $H_{\text{lower}}$  can be also calculated as follows:

$$H_{\text{lower}} = \left( \frac{f_{\text{glass}}}{H_{\text{glass}}} + \frac{f_{\text{alumina}}}{H_{\text{alumina}}} \right)^{-1},$$

where  $H_{\text{glass}}$  was obtained experimentally using glass without  $\text{Al}_2\text{O}_3$  and  $H_{\text{alumina}}$  was taken from a previous study [33].

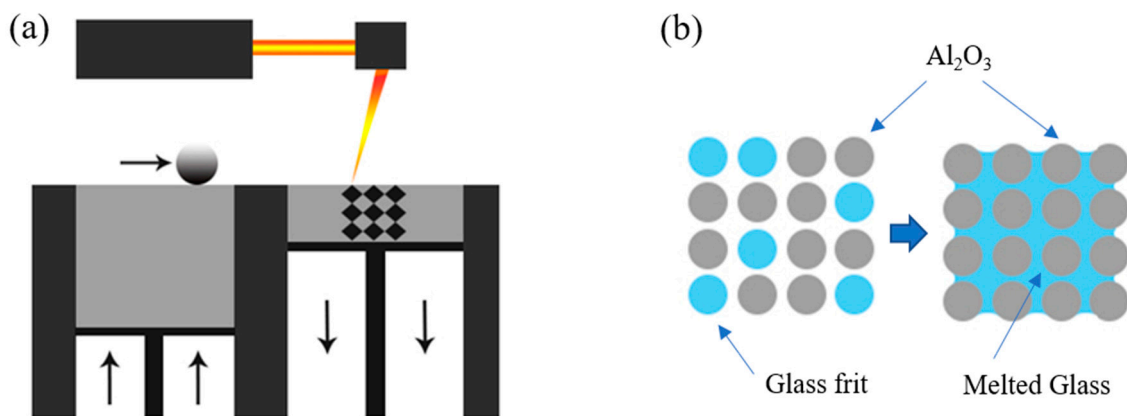


**Figure 1.** Mechanism of density improvement of glass/ $\text{Al}_2\text{O}_3$  composite: (a) 3D printing powder bed fusion (PBF) process; and (b) schematic of glass frit/ $\text{Al}_2\text{O}_3$  composite.

To demonstrate the feasibility of our approach for manufacturing high-density products, after powder bedding, we transversely irradiated the powder with a 50- $\mu\text{m}$ -diameter laser beam in a hatch pattern with a width of 500  $\mu\text{m}$  and size of 50 mm to fabricate each layer. Next, after laminating the powder to 1 mm or less, the powder sample was laser-irradiated along the longitudinal direction. The above process was repeated to fabricate a continuously layered scaffold. The overall experimental processes are shown in Figure 2.

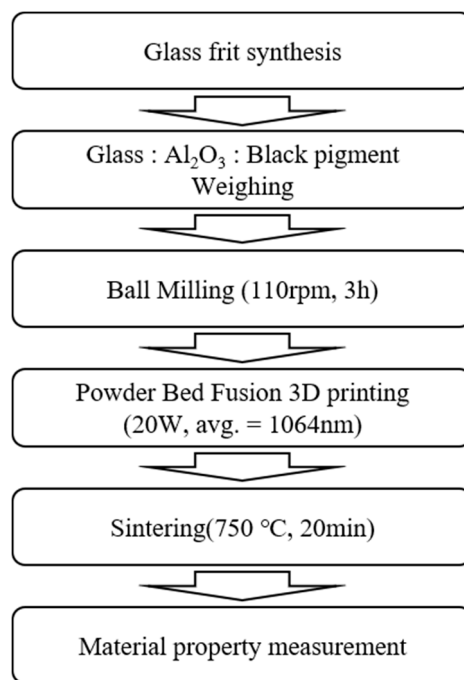


**Figure 2.** Process flow for glass/ $\text{Al}_2\text{O}_3$  composite fabrication and property measurement.

### 3. Results and Discussion

#### 3.1. Results of Glass Sintering at 750 °C

The composition of the glass frit used for low-temperature sintering below 800 °C was  $\text{SiO}_2\text{-B}_2\text{O}_3\text{-RO}$  ( $\text{R} = \text{Ba}, \text{Zn}$ ). After melting for 1 h at 1400 °C in an alumina crucible, the glass frit was quenched in a brass mold and crushed into particles of 50  $\mu\text{m}$  or smaller. Figure 3a shows an SEM photograph of the glass frit. The fabricated glass frit was quenched and crushed to particle sizes of  $\sim 10 \mu\text{m}$  to inspect the particle shape and glass phase in the crushed form. Figure 3b shows the XRD results for the crushed glass frit; the sample is clearly observed to exhibit amorphousness, with no special crystalline peaks present.

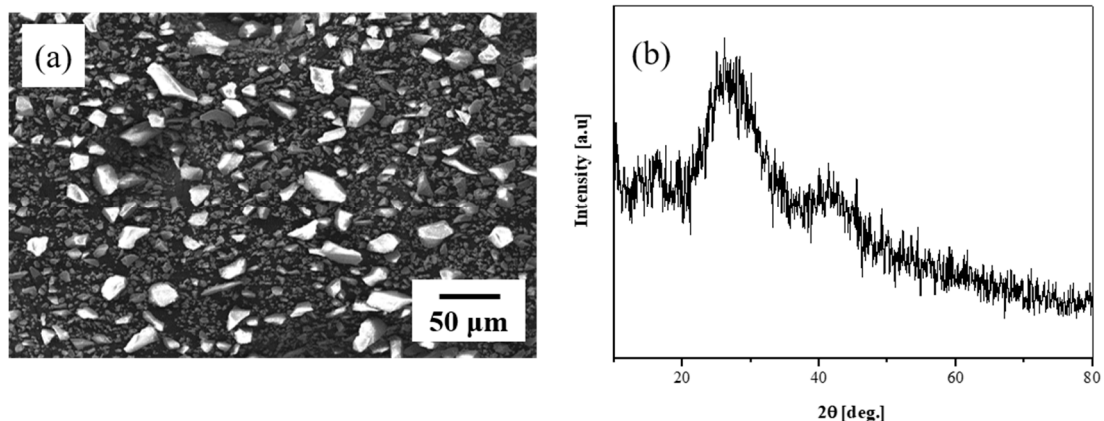


**Figure 3.** (a) Scanning electron microscope (SEM) image and (b) X-ray diffraction (XRD) results of synthesized glass frit.

Figure 4 shows the measurements of the glass transition and softening points of the glass frit as per differential thermal analysis (DTA). We note that for low-temperature-sintered glass, the transition

point is 589.54 °C and the softening point is 671.47 °C. No crystallization peaks are observed, which indicates that amorphous glass was synthesized.

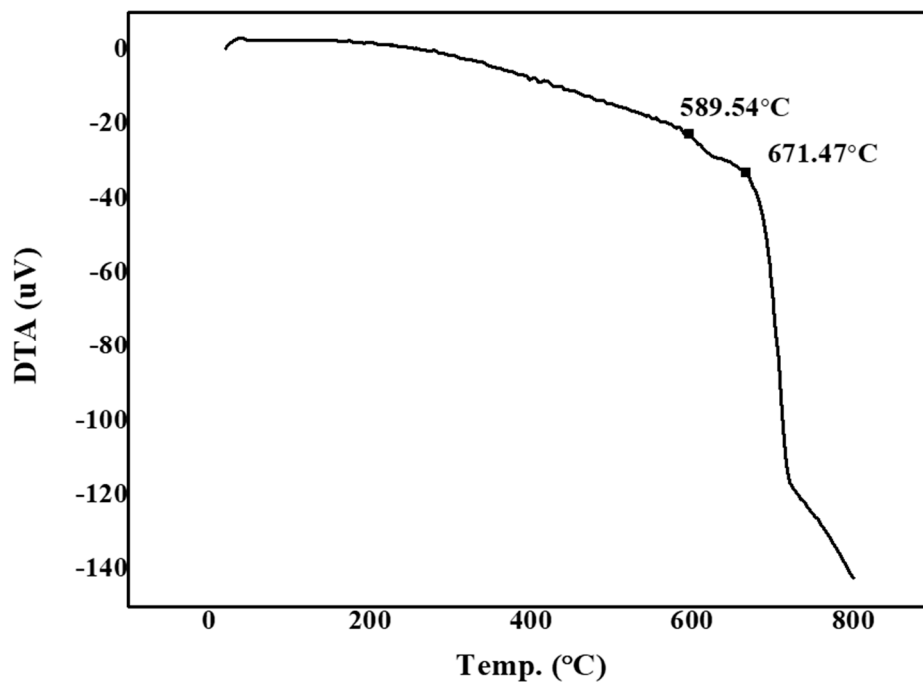


**Figure 4.** Differential thermal analysis (DTA) results of  $\text{SiO}_2\text{-B}_2\text{O}_3\text{-RO}$  glass frit ( $R = \text{Ba, Zn}$ ).

To examine the sample thermal behavior as a function of the glass temperature, we raised the temperature from room temperature to 800 °C in intervals of 5 °C/min. Figure 5 shows the corresponding high-temperature microscope images. We note that there is almost no shrinkage in the range from 600 to 650 °C. At 700 °C, shrinkage is observed to occur from the top of the sintered body to the outer vertex; a volume shrinkage of 33% and length shrinkage of 20% occurs at this temperature. At 750 °C, the frit exhibits a round-shaped spread, and a volume shrinkage of 48% (length shrinkage of 29%) is observed, which indicates that sintering is performed. At 800 °C, the volume shrinkage reaches 56% (length shrinkage of 47%), and complete melting and spreading are observed. This result demonstrates that the post-heat-treatment temperature of 750 °C is adequate to ensure sufficient sinterability of the glass frit.

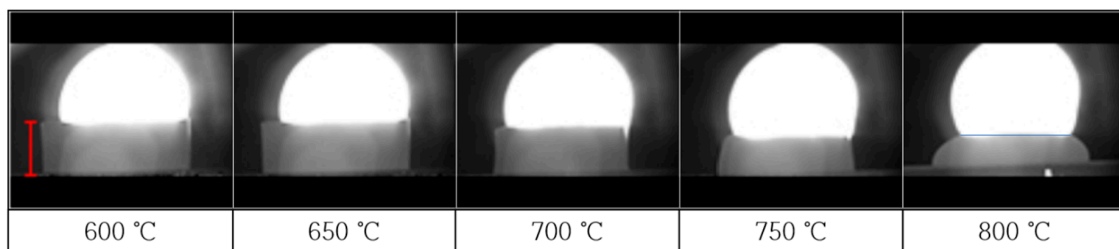


**Figure 5.** High-temperature microscope (HTM) images of  $\text{SiO}_2\text{-B}_2\text{O}_3\text{-RO}$  glass frit ( $R = \text{Ba, Zn}$ ) (Heating rate = 5 °C/min).

Our particle-size measurements with a particle size analyzer (PSA) (Mastersizer 3000, Malvern, UK) confirmed that a homogeneous powder with  $d_{50}$  and  $d_{\text{max}}$  particle sizes of 15 and 50  $\mu\text{m}$ , respectively, were obtained (Table 1). This  $d_{50}$  particle size is equivalent to that of commercial 3D printing material, and the uniformity is expected to improve when mixed with  $\text{Al}_2\text{O}_3$ .

**Table 1.** Thermal properties and particle sizes of developed glass.

Classification	Unit	Value
Transition Temperature	°C	589
Softening Temperature	°C	671
Particle Size ( $d_{50}$ )	$\mu\text{m}$	15
Particle Size ( $d_{\text{max}}$ )	$\mu\text{m}$	50

### 3.2. Mixing Ratio of Fabricated Glass/ $\text{Al}_2\text{O}_3$ Composite and Mechanical-Property Evaluation

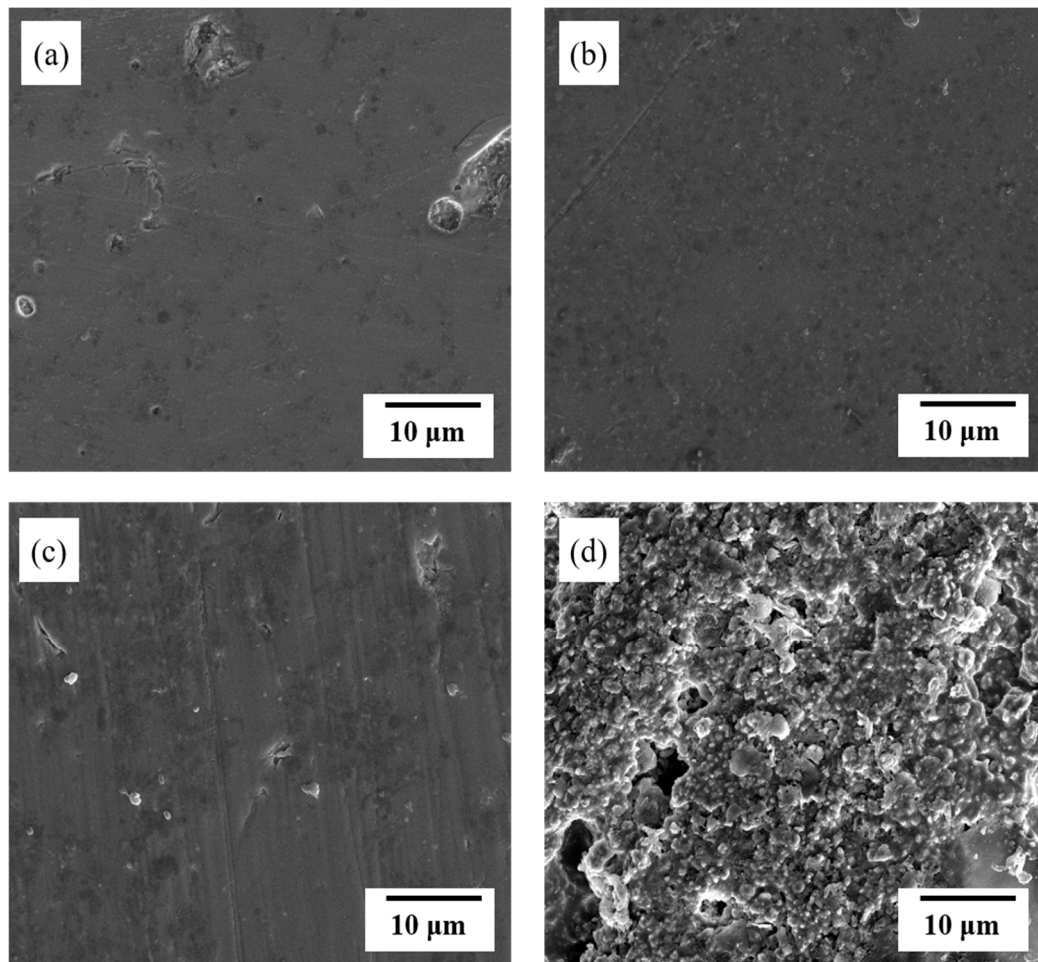
To find the optimal composition ratio suitable for 3D printing, we considered the glass/ $\text{Al}_2\text{O}_3$  mixing ratios of 60:40, 70:30, 80:20, and 90:10 wt %. After bedding, the powder was irradiated with the laser (Figure 6), and a 3D sample with dimensions of 80 mm was fabricated for each mixing ratio.

**Figure 6.** Optical microscope image of melt glass frit obtained with laser scanning.

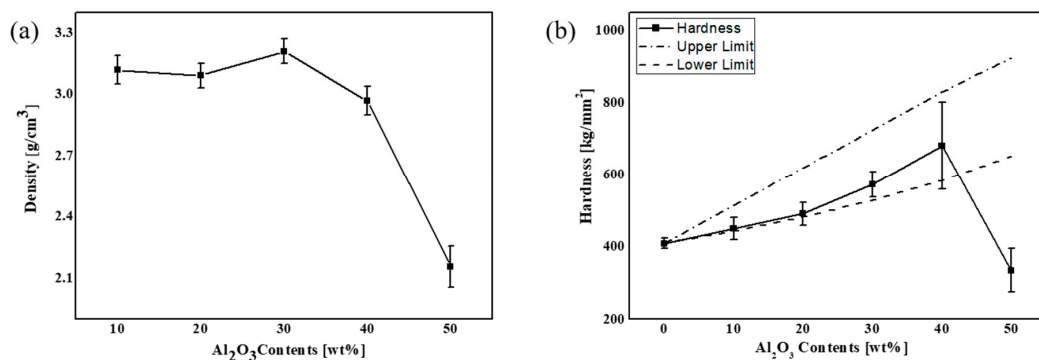
The produced shape was sintered at 750 °C for 20 min. Figure 7 shows the SEM images of the surface of the various glass/ $\text{Al}_2\text{O}_3$  composites after polishing. From Figure 7a, we can clearly observe the glass-like properties of the sample due to the presence of 90 wt % glass mixed with 10 wt %  $\text{Al}_2\text{O}_3$  content. Figure 7b shows the SEM image of the surface of the sample with 80 wt % glass and 20 wt %  $\text{Al}_2\text{O}_3$ ; we can clearly observe a sintered form, wherein the glass has melted and enveloped the  $\text{Al}_2\text{O}_3$  particles. As  $\text{Al}_2\text{O}_3$  exhibits excellent reactivity with glass, no air bubbles are observed. In Figure 7c, corresponding to the 70:30 wt % sample, no air bubbles are observed, and the surface density is satisfactory even when the  $\text{Al}_2\text{O}_3$  content of the sample is increased to 30 wt %. In Figure 7d, corresponding to the sample with a low glass content of 60 wt % and 40 wt %  $\text{Al}_2\text{O}_3$ , the glass does not sufficiently envelop the  $\text{Al}_2\text{O}_3$  particles. This insufficient coverage results in the formation of open pores, which affords a sample with insufficient density.

Figure 8 shows the plots of the density and hardness of the various samples as functions of the  $\text{Al}_2\text{O}_3$  content. From Figure 8a, we note that with an increase in the  $\text{Al}_2\text{O}_3$  content and a decrease in the glass content, the molten glass does not sufficiently envelop the  $\text{Al}_2\text{O}_3$  particles, thereby leading to a density decrease. Here, we note that the densities of the glass,  $\text{Al}_2\text{O}_3$ , and black pigment were 3.20 g/cm<sup>3</sup>, 3.95 g/cm<sup>3</sup>, and 5.6 g/cm<sup>3</sup>, respectively, and the theoretical density of the composite was obtained in proportion to the lever rule. The calculated theoretical and experimental densities are listed in Table 2. We note that the overall density remains high at ~95.3% of the theoretical density of 3.42 g/cm<sup>3</sup> for the  $\text{Al}_2\text{O}_3$  range of 10% to 30%, and the density significantly reduces when the  $\text{Al}_2\text{O}_3$  content increases to 40%; this result corresponds to the SEM images in Figure 7. Therefore, the efficiency of 3D printing can be maximized by setting the  $\text{Al}_2\text{O}_3$  content to 30%, which yields the highest density (95.3%). Meanwhile, from Figure 8b, we note that the hardness increases with increase in the  $\text{Al}_2\text{O}_3$  content; the hardness increases from 452 HV for the  $\text{Al}_2\text{O}_3$  content of 10% to 772 HV for the  $\text{Al}_2\text{O}_3$  content of 40%, and subsequently it decreases to 337 HV for the  $\text{Al}_2\text{O}_3$  content of 50%. This is because

there is an insufficient amount of glass available to envelop the  $\text{Al}_2\text{O}_3$  in the glass/ $\text{Al}_2\text{O}_3$  composite as the  $\text{Al}_2\text{O}_3$  content increases. The experimentally obtained results were closer to the estimated lower bound, which is thought to be related to insufficient densities of the experimental samples. The average hardness values for the composite with  $\text{Al}_2\text{O}_3$  ranging from 10% to 40% were within the upper and lower bounds but the value for 50% was out of the estimated bound, which can be explained from the relatively low experimental density. Therefore, from Figure 7a,b and Figure 8, we can confirm that the  $\text{Al}_2\text{O}_3$  content of 30% is the most suitable for 3D printing.



**Figure 7.** Scanning electron microscope (SEM) images of polished surface of (a) 90:10, (b) 80:20, (c) 70:30, and (d) 60:40 wt % glass/ $\text{Al}_2\text{O}_3$  composite samples.



**Figure 8.** (a) Density and (b) hardness of sintered glass mixed with  $\text{Al}_2\text{O}_3$  as functions of  $\text{Al}_2\text{O}_3$  content.

**Table 2.** Theoretical and experimental densities of composites.

Al <sub>2</sub> O <sub>3</sub> Content (wt % (vol %))	Theoretical Density of Composite (g/cm <sup>3</sup> )	Experimental Density (% of Theoretical Density)
10 (08)	3.28	94.8
20 (17)	3.35	92.5
30 (25)	3.42	95.3
40 (34)	3.49	85.1
50 (44)	3.56	60.7

Figure 9 shows the XRD analysis results of the glass/Al<sub>2</sub>O<sub>3</sub> composites. For 10 wt % Al<sub>2</sub>O<sub>3</sub>, the amorphous phase is most apparent, although Al<sub>2</sub>O<sub>3</sub> peaks are also observed. With increase in the Al<sub>2</sub>O<sub>3</sub> content from 20 wt % to 50 wt %, the number of crystalline Al<sub>2</sub>O<sub>3</sub> peaks increases. This result confirms that no secondary phase is generated by reactions between the amorphous glass and crystalline Al<sub>2</sub>O<sub>3</sub>.

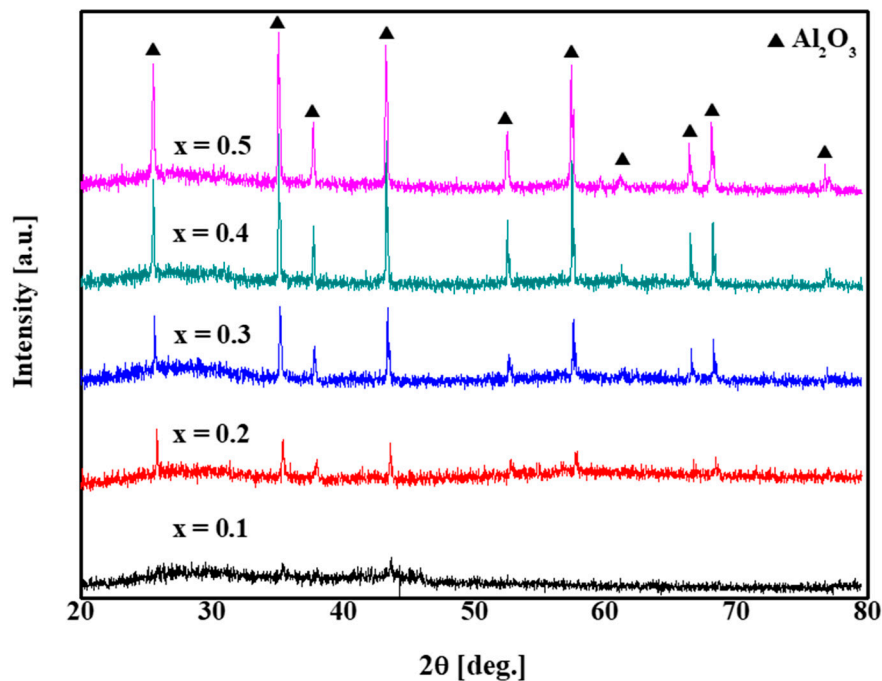


**Figure 9.** X-ray diffraction (XRD) results of [xglass/(1 - x)Al<sub>2</sub>O<sub>3</sub>] composite samples for x = 0.1 – 0.5 Al<sub>2</sub>O<sub>3</sub>.

Figure 10 shows the image of a scaffold constructed using the glass/Al<sub>2</sub>O<sub>3</sub> composite with 30% Al<sub>2</sub>O<sub>3</sub>. Figure 10a shows the scaffold image after 50 μm laser irradiation in a hatch pattern. In this phase of the study, laser irradiation was performed along the transverse direction after powder bedding. The platform holding the scaffold was next lowered along the Z-axis, the powder was bedded to 1 mm or less, and the laser was used to irradiate the powder layer along the longitudinal direction. This process was continuously repeated. Each line was about 500 μm in length, and after several layering processes, a continuous layered scaffold with a size of ~5 mm was fabricated. Printing was performed as the glass frit melted and enveloped the Al<sub>2</sub>O<sub>3</sub>. The sample with 70:30 wt % of glass:Al<sub>2</sub>O<sub>3</sub> was used in this case. Figure 10b shows the highly dense scaffold fabricated after heat treatment at 750 °C. A 3D shape was fabricated out of this ceramic material by laser-irradiating only the powder with no binder. As there was no debinding process involved, it was possible to produce a complex 3D structure with high density.



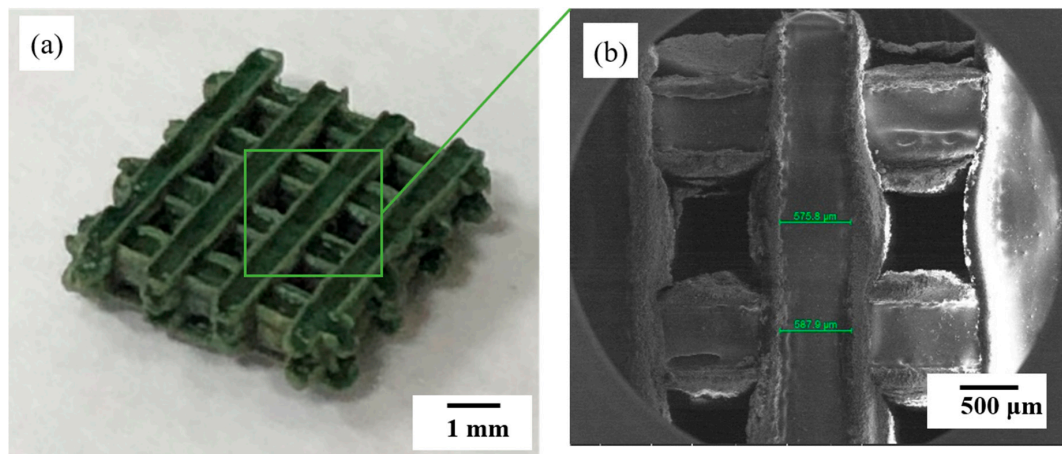


**Figure 10.** (a) Optical and (b) scanning electron microscope (SEM) images of a 3D scaffold manufactured by powder bed fusion (PBF).

#### 4. Conclusions

In this study, we fabricated a glass/ $\text{Al}_2\text{O}_3$  composite using powder bed fusion (PBF) 3D printing. Laser 3D printing, which is generally used for metals and more recently tested with glass, was applied to a ceramic material to fabricate a composite molded body without polymer binder. The fabricated glass frit (particle size  $d_{\text{max}} < 50 \mu\text{m}$ ) exhibited no crystallinity as per our XRD analysis. The frit was subsequently mixed with commercial  $\text{Al}_2\text{O}_3$  at ratios ranging from 90:10 wt % to 50:50 wt %, with 1 wt % to 3 wt % black pigment being added for enhancing laser-light absorption. After fabricating the molded body by laser-irradiating the powder at each mixing ratio, we measured the resulting hardness. A subsequent XRD analysis confirmed that the glass and crystalline  $\text{Al}_2\text{O}_3$  phases did not react with each other. The composite with glass: $\text{Al}_2\text{O}_3 = 70:30$  wt % exhibited a hardness of  $578 \text{ kg/mm}^2$  and density of  $3.26 \text{ g/cm}^3$ ; this ratio was determined as the optimum mixing ratio. This composite sample was irradiated by a 20 W, 1060 nm wavelength fiber laser (MLPS-20, Germany) to obtain a sintered composite. To apply the PBF method and demonstrate the practicability of using the composite, after bedding the glass: $\text{Al}_2\text{O}_3 = 70:30$  wt % powder, we transversely irradiated the sample with a 50- $\mu\text{m}$ -diameter laser beam in a hatch pattern with a width of  $500 \mu\text{m}$  and size of 50 mm to fabricate one layer. Next, after lamination to 1 mm or less, the powder was irradiated by the laser along the longitudinal direction. The above process was repeated to fabricate a high-density continuously layered glass/ $\text{Al}_2\text{O}_3$  composite 3D scaffold with a size of 80 mm. The successful fabrication of this scaffold indicates the practical applicability of our approach to manufacture high-density glass/ $\text{Al}_2\text{O}_3$ -composite-based products.

**Author Contributions:** B.H.B., J.W.L., J.M.C. and I.-W.K. conducted the experimental and analytical studies. C.-B.Y. and H.-D.J. designed and supervised the project and wrote the manuscript. All authors have read and agreed to the published version of the manuscript.

**Funding:** This study was funded by The Catholic University of Korea, Research Fund, 2020 and the Basic Science Research Program [No. 2018R1C1B6001003] through the National Research Foundation of Korea funded by the Korean government (MSIT) and the Ministry of Trade, Industry and Energy (MOTIE) of Korea and conducted under the “Competency Development Program for Industry Specialists,” undertaken by the Korean Institute for Advancement of Technology (KIAT) (No. P0002007, HRD program for 3D Printing based on 3D Printing Materials).

**Conflicts of Interest:** The authors declare no conflict of interest.

#### References

1. Graf, D.; Burchard, S.; Crespo, J.; Megnin, C.; Gutsch, S.; Zacharias, M.; Hanemann, T. Influence of  $\text{Al}_2\text{O}_3$  nanoparticle addition on a uv cured polyacrylate for 3d inkjet printing. *Polymers* **2019**, *11*, 633. [[CrossRef](#)] [[PubMed](#)]

2. Lee, J.; Lee, H.; Cheon, K.-H.; Park, C.; Jang, T.-S.; Kim, H.-E.; Jung, H.-D. Fabrication of poly (lactic acid)/Ti composite scaffolds with enhanced mechanical properties and biocompatibility via fused filament fabrication (fff)-based 3d printing. *Addit. Manuf.* **2019**, *30*, 100883. [[CrossRef](#)]
3. Jung, H.-D.; Jang, T.-S.; Lee, J.E.; Park, S.J.; Son, Y.; Park, S.-H. Enhanced bioactivity of titanium-coated polyetheretherketone implants created by a high-temperature 3d printing process. *Biofabrication* **2019**, *11*, 045014. [[CrossRef](#)] [[PubMed](#)]
4. Atzeni, E.; Iuliano, L.; Minetola, P.; Salmi, A. Redesign and cost estimation of rapid manufactured plastic parts. *Rapid Prototyp. J.* **2010**. [[CrossRef](#)]
5. Atzeni, E.; Salmi, A. Economics of additive manufacturing for end-useable metal parts. *Int. J. Adv. Manuf. Technol.* **2012**, *62*, 1147–1155. [[CrossRef](#)]
6. Kotz, F.; Arnold, K.; Bauer, W.; Schild, D.; Keller, N.; Sachsenheimer, K.; Nargang, T.M.; Richter, C.; Helmer, D.; Rapp, B.E. Three-dimensional printing of transparent fused silica glass. *Nature* **2017**, *544*, 337–339. [[CrossRef](#)]
7. Chen, Z.; Li, Z.; Li, J.; Liu, C.; Lao, C.; Fu, Y.; Liu, C.; Li, Y.; Wang, P.; He, Y. 3d printing of ceramics: A review. *J. Eur. Ceram. Soc.* **2019**, *39*, 661–687. [[CrossRef](#)]
8. Okada, A. Automotive and industrial applications of structural ceramics in japan. *J. Eur. Ceram. Soc.* **2008**, *28*, 1097–1104. [[CrossRef](#)]
9. Rödel, J.; Kounga, A.B.; Weissenberger-Eibl, M.; Koch, D.; Bierwisch, A.; Rossner, W.; Hoffmann, M.J.; Danzer, R.; Schneider, G. Development of a roadmap for advanced ceramics: 2010–2025. *J. Eur. Ceram. Soc.* **2009**, *29*, 1549–1560. [[CrossRef](#)]
10. Baek, J.; Lee, H.; Jang, T.-S.; Song, J.; Kim, H.-E.; Jung, H.-D. Incorporation of calcium sulfate dihydrate into hydroxyapatite microspheres to improve the release of bone morphogenetic protein-2 and accelerate bone regeneration. *ACS Biomater. Sci. Eng.* **2018**, *4*, 846–856. [[CrossRef](#)]
11. Klein, J.; Stern, M.; Franchin, G.; Kayser, M.; Inamura, C.; Dave, S.; Weaver, J.C.; Houk, P.; Colombo, P.; Yang, M. Additive manufacturing of optically transparent glass. *3D Print. Addit. Manuf.* **2015**, *2*, 92–105. [[CrossRef](#)]
12. Luo, J.; Pan, H.; Kinzel, E.C. Additive manufacturing of glass. *J. Manuf. Sci. Eng.* **2014**, *136*. [[CrossRef](#)]
13. Luo, J.; Bender, T.; Bristow, D.A.; Landers, R.G.; Goldstein, J.T.; Urbas, A.M.; Kinzel, E.C. *Bubble Formation in Additive Manufacturing of Borosilicate Glass, Proceedings of the 2016 Annual International Solid Freeform Fabrication Symposium, Austin, TX, USA, 8–10 August 2016*; University of Texas: Austin, TX, USA, 2016; pp. 998–1003.
14. Luo, J.; Gilbert, L.J.; Qu, C.; Landers, R.G.; Bristow, D.A.; Kinzel, E.C. Additive manufacturing of transparent soda-lime glass using a filament-fed process. *J. Manuf. Sci. Eng.* **2017**, *139*. [[CrossRef](#)]
15. Luo, J.; Gilbert, L.J.; Bristow, D.A.; Landers, R.G.; Goldstein, J.T.; Urbas, A.M.; Kinzel, E.C. Additive manufacturing of glass for optical applications. In *Laser 3D Manufacturing III*; International Society for Optics and Photonics: Bellingham, WA, USA, 2016; p. 97380Y.
16. Schmid, C. *The Chemistry of Inkjet Inks*; World Scientific Publishing: Hackensack, NJ, USA, 2008; p. 123.
17. Ligon, S.C.; Liska, R.; Stampfl, J.; Gurr, M.; Mülhaupt, R. Polymers for 3d printing and customized additive manufacturing. *Chem. Rev.* **2017**, *117*, 10212–10290. [[CrossRef](#)]
18. Dorfinger, P.; Stampfl, J.; Liska, R. Toughening of photopolymers for stereolithography (sl). In *Materials Science Forum*; Trans Tech Publ: Schwyz, Switzerland, 2015; pp. 53–59.
19. Nguyen, D.T.; Meyers, C.; Yee, T.D.; Dudukovic, N.A.; Destino, J.F.; Zhu, C.; Duoss, E.B.; Baumann, T.F.; Suratwala, T.; Smay, J.E. 3d-printed transparent glass. *Adv. Mater.* **2017**, *29*, 1701181. [[CrossRef](#)]
20. Thostenson, E.T.; Li, C.; Chou, T.-W. Nanocomposites in context. *Compos. Sci. Technol.* **2005**, *65*, 491–516. [[CrossRef](#)]
21. Johnsen, B.; Kinloch, A.; Mohammed, R.; Taylor, A.; Sprenger, S. Toughening mechanisms of nanoparticle-modified epoxy polymers. *Polymer* **2007**, *48*, 530–541. [[CrossRef](#)]
22. Wu, Z.; Liu, W.; Wu, H.; Huang, R.; He, R.; Jiang, Q.; Chen, Y.; Ji, X.; Tian, Z.; Wu, S. Research into the mechanical properties, sintering mechanism and microstructure evolution of Al<sub>2</sub>O<sub>3</sub>-ZrO<sub>2</sub> composites fabricated by a stereolithography-based 3d printing method. *Mater. Chem. Phys.* **2018**, *207*, 1–10. [[CrossRef](#)]
23. Santoliquido, O.; Colombo, P.; Ortona, A. Additive manufacturing of ceramic components by digital light processing: A comparison between the “bottom-up” and the “top-down” approaches. *J. Eur. Ceram. Soc.* **2019**, *39*, 2140–2148. [[CrossRef](#)]

24. Zhou, M.; Liu, W.; Wu, H.; Song, X.; Chen, Y.; Cheng, L.; He, F.; Chen, S.; Wu, S. Preparation of a defect-free alumina cutting tool via additive manufacturing based on stereolithography—optimization of the drying and debinding processes. *Ceram. Int.* **2016**, *42*, 11598–11602. [[CrossRef](#)]
25. Crosby, A.J.; Lee, J.Y. Polymer nanocomposites: The “nano” effect on mechanical properties. *Polym. Rev.* **2007**, *47*, 217–229. [[CrossRef](#)]
26. Ash, B.J.; Siegel, R.W.; Schadler, L.S. Mechanical behavior of alumina/poly (methyl methacrylate) nanocomposites. *Macromolecules* **2004**, *37*, 1358–1369. [[CrossRef](#)]
27. Khmyrov, R.; Grigoriev, S.; Okunkova, A.; Gusarov, A. On the possibility of selective laser melting of quartz glass. *Phys. Procedia* **2014**, *56*, 345–356. [[CrossRef](#)]
28. Khmyrov, R.; Protasov, C.; Grigoriev, S.; Gusarov, A. Crack-free selective laser melting of silica glass: Single beads and monolayers on the substrate of the same material. *Int. J. Adv. Manuf. Technol.* **2016**, *85*, 1461–1469. [[CrossRef](#)]
29. Datsiou, K.C.; Saleh, E.; Spirrett, F.; Goodridge, R.; Ashcroft, I.; Eustice, D. Additive manufacturing of glass with laser powder bed fusion. *J. Am. Ceram. Soc.* **2019**, *102*, 4410–4414. [[CrossRef](#)]
30. Duan, B.; Wang, M.; Zhou, W.Y.; Cheung, W.L.; Li, Z.Y.; Lu, W.W. Three-dimensional nanocomposite scaffolds fabricated via selective laser sintering for bone tissue engineering. *Acta Biomater.* **2010**, *6*, 4495–4505. [[CrossRef](#)]
31. Wilkes, J.; Hagedorn, Y.C.; Meiners, W.; Wissenbach, K. Additive manufacturing of ZrO<sub>2</sub>-Al<sub>2</sub>O<sub>3</sub> ceramic components by selective laser melting. *Rapid Prototyp. J.* **2013**. [[CrossRef](#)]
32. Awasthi, S.; Maurya, R.; Pandey, C.P.; Balani, K. Interfacial mechanics of carbonaceous reinforcements in electrophoretically deposited nickel coatings. *Surf. Coat. Technol.* **2017**, *310*, 79–86. [[CrossRef](#)]
33. Asano, K. Preparation of alumina fiber-reinforced aluminum by squeeze casting and their machinability. *Mater. Manuf. Process.* **2015**, *30*, 1312–1316. [[CrossRef](#)]



© 2020 by the authors. Licensee MDPI, Basel, Switzerland. This article is an open access article distributed under the terms and conditions of the Creative Commons Attribution (CC BY) license (<http://creativecommons.org/licenses/by/4.0/>).